Compensated Ferrimagnetism in the Zero-Moment Heusler Alloy Mn_3Al

Michelle E. Jamer,[1,2] Yung Jui Wang,[2] Gregory M. Stephen,[2] Ian J. McDonald,[3,4] Alexander J. Grutter,[1] George E. Sterbinsky,[5] Dario A. Arena,[6] Julie A. Borchers,[1] Brian J. Kirby,[1] Laura H. Lewis,[3,4] Bernardo Barbiellini,[2] Arun Bansil,[2] and Don Heiman[2]

[1]*NIST Center for Neutron Research, National Institute of Standards and Technology, Gaithersburg, Maryland 20899, USA*
[2]*Department of Physics, Northeastern University, Boston, Massachusetts 02115, USA*
[3]*Department of Chemical Engineering, Northeastern University, Boston, Massachusetts 02115, USA*
[4]*Department of Mechanical and Industrial Engineering, Northeastern University, Boston, Massachusetts 02115, USA*
[5]*Advanced Photon Source, Argonne National Laboratory, Argonne, Illinois 60439, USA*
[6]*Department of Physics, University of South Florida, Tampa, Florida 33620, USA*

(Received 22 February 2017; revised manuscript received 17 May 2017; published 30 June 2017)

While antiferromagnets have been proposed as components to limit stray magnetic fields, their inability to be spin polarized inhibits their use in spintronic devices. Compensated ferrimagnets are a unique solution to this dilemma since they have zero net moment, but their nonsymmetric density of states allows the achievement of high spin polarization. Density-functional theory predicts Mn_3Al in the $D0_3$ structure to be fully compensated and retain half-metallicity at room temperature. In this work, 50-nm Mn_3Al thin films are synthesized using molecular beam epitaxy and annealed at various temperatures in order to investigate their magnetic properties. Magnetometry measurements confirm the high Curie temperature of 605 K. Polarized-neutron reflectometry (PNR) indicates a low net magnetic moment, along with depth profiles of the structure and magnetization. From the PNR data, a saturation moment of $0.11 \pm 0.04\ \mu_B/\mathrm{f.u.}$ is extracted, confirming the nominal zero moment present in these thin films.

DOI: 10.1103/PhysRevApplied.7.064036

I. INTRODUCTION

For future spintronic devices, it will be advantageous to limit extraneous magnetic interactions, which can negatively impact the spin polarization of electrons. While antiferromagnets have been proposed as components in various spintronic devices to eliminate these stray fields, the antiferromagnetic band structure prohibits spin polarization of the bulk carriers [1]. Compensated ferrimagnets provide a unique solution to this problem, with a net zero moment and a band structure which allows for spin-polarized carriers [2–4]. Recently, several Heusler materials have been suggested as spin-polarized compensated ferrimagnets [5–7]. Here we investigate nominally zero-moment Mn_3Al thin films, which are synthesized using molecular beam epitaxy (MBE) on GaAs substrates.

It is interesting to compare the magnetic properties of V_3Al and Mn_3Al, which share the same $D0_3$ crystal structure. Mn_3Al exhibits ferrimagnetism, while V_3Al is antiferromagnetic. Moreover, the asymmetric electronic properties of Mn_3Al allow the system to become half-metallic, but the symmetric electronic structure of V_3Al prohibits spin polarization. The G-type antiferromagnetic structure of V_3Al is shown in Fig. 1 (lower left) [8,9]. The $D0_3$ Mn_3Al structure is based on the full Heusler space group $Fm\bar{3}m$, which has the formula Y_2XZ where X and Y are equal, leading to the formula X_3Z. Figure 1 (lower right) illustrates two distinguishable Mn positions in Mn_3Al: $\mathrm{Mn}(X)$ atoms at the Wyckoff $4b$ $(\frac{1}{2}, \frac{1}{2}, \frac{1}{2})$ positions and $\mathrm{Mn}(Y)$ atoms at the $8c$ $(\frac{1}{4}, \frac{1}{4}, \frac{1}{4})$ positions. Note that there are twice as many $\mathrm{Mn}(Y)$ atoms as there are $\mathrm{Mn}(X)$ atoms and that they occupy the octahedral sites surrounded by eight $\mathrm{Mn}(X)$ atoms. The Z atom occupies the $4a$ (0,0,0) position labeled $\mathrm{Al}(Z)$ [10]. Recently, $D0_3$-type V_3Al was synthesized and determined to behave as a gapless semiconductor, where Fig. 1 (upper left) shows both the majority (red) and minority (blue) bands in the DOS are symmetric, prohibiting spin polarization [11,12]. In the case of Mn_3Al, Mn moments are predicted to order into a compensated ferrimagnet [4,13] shown in Fig. 1 (right lower), which allows the DOS to behave as a half-metal as seen in Fig. 1 (upper right) [14–16].

Compensated ferrimagnets are ideal for room-temperature high-density magnetic memory applications. Mn_3Al is especially promising for giant tunable exchange-bias applications, since Mn has a strong localized magnetic moment [17]. Developing Mn_3Al for exchange-bias applications can allow for an extremely large exchange bias at room temperature in spin-valve sensors without the use of rare-earth magnets, as previously shown in Mn-Ga systems [17]. In addition, the low net magnetization, which prevents the demagnetization of surrounding components and limits stray field interactions, is expected to lead to suppressed damping

 © 2017 American Physical Society

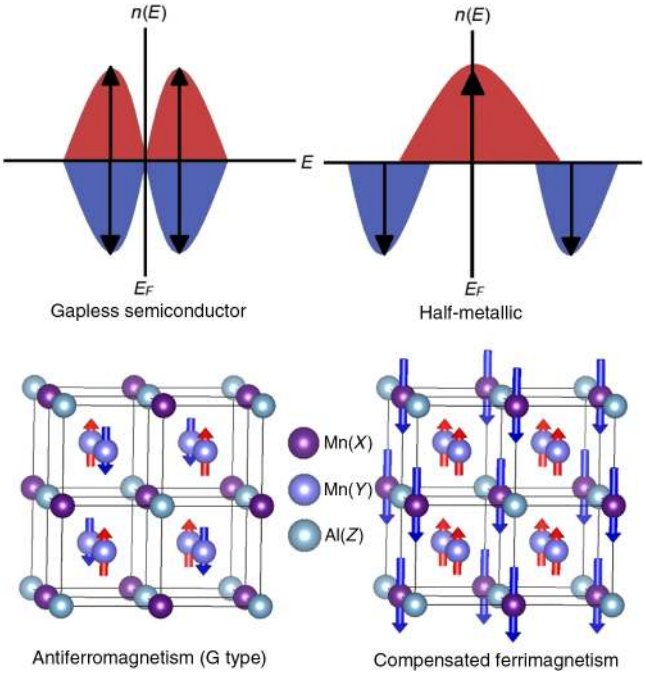

FIG. 1. Schematic density of states and magnetic structure of $D0_3$ compounds. (Left upper) Density of states of a gapless semiconductor showing the majority and minority bands. (Left lower) G-type antiferromagnetic structure of V_3Al. (Right upper) Density-of-states schematic of half-metallic materials. (Right lower) Proposed magnetic lattice of Mn_3Al which is a compensated ferrimagnet.

and high switching speeds. These superior properties are advantageous for terahertz spin-torque oscillators [18].

II. ELECTRONIC STRUCTURE OF Mn_3Al

First-principles calculations of the band structure of Mn_3Al are performed within the framework of the density-functional theory (DFT) by using projector-augmented-wave pseudopotentials [19] as implemented in the VASP package [20]. The generalized-gradient approximation (GGA) [21] is used for treating exchange-correlation effects. The GGA plays a crucial role in stabilizing magnetic structures compared to the local-spin-density approximation [22]. The Brillouin zone is integrated by using a $16 \times 16 \times 16$ k-point mesh with 360-eV cutoff energy.

For the cubic $Fm\bar{3}m$ $D0_3$ phase, the lattice parameter of $a = 5.79$ Å is determined by minimizing the total energy using the fitting method of Murnaghan's equation of state [23,24]. The corresponding magnetic structure is found to be a compensated ferrimagnet as shown in Fig. 1 (lower right) in which the Mn(X), Mn(Y), and Al atomic sites carry magnetic moments of -2.79, 1.40, and -0.02 μ_B, respectively, and the net magnetic moment summed over all atomic sites is nearly fully compensated. The computed lattice constant and magnetic structure are consistent with previous calculations [7].

Figure 2 shows the computed spin-polarized partial density of states (PDOS) per atom projected on the distinct atomic sites of Mn_3Al. The Fermi energy is set at 0 eV. Figures 2(a)–2(d) show Mn(X)-d, Mn(Y)-d, and Al-p PDOS of the cubic phase with lattice constant $a = 5.79$ Å. The magnetic moments mostly develop on the Mn(X) and Mn(Y) sites. The asymmetric shape of the spin-resolved PDOS indicates that the Mn(X) sites host spin-down majority states, while the Mn(Y) sites host spin-up majority states. Compared to the highly spin-polarized effects on the Mn(X) and Mn(Y) sites, the PDOS on the Al atoms exhibit much less spin polarization. It is interesting to note that the PDOS at the Mn(X), Mn(Y), and Al sites between -0.2 and 0.2 eV near the Fermi energy are mostly composed of spin-down states, leading to a very high degree of spin

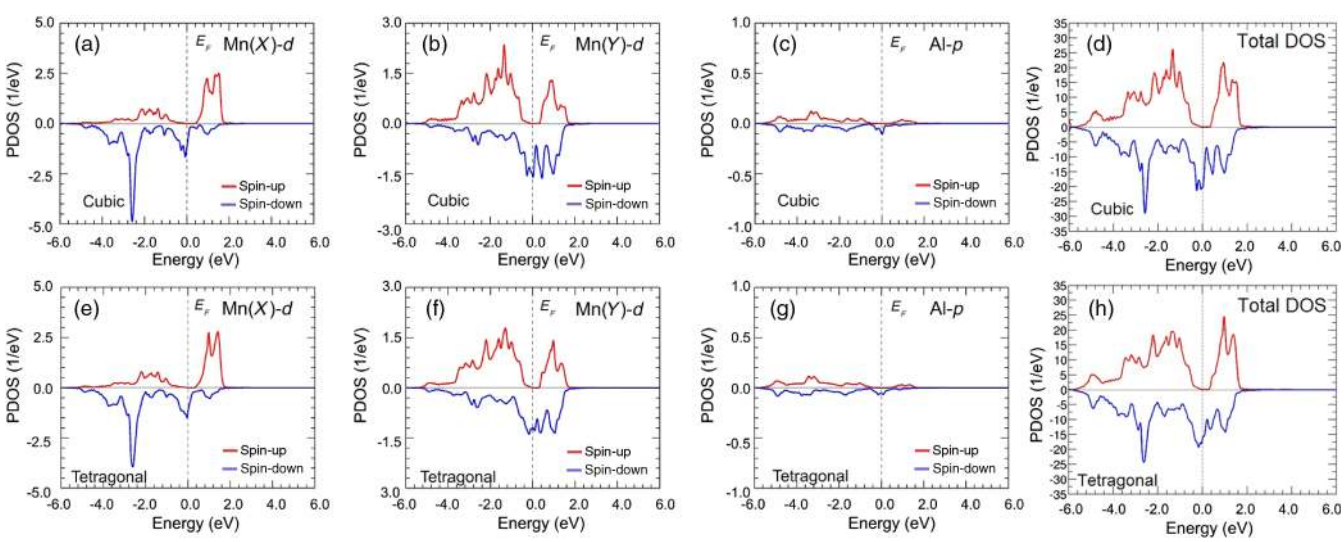

FIG. 2. Spin-polarized PDOS per atom on the distinct atomic sites of Mn_3Al. Fermi energy is set at 0 eV. (a)–(d) Mn(X)-d, Mn(Y)-d, and Al-p PDOS of the cubic phase with lattice constant $a = 5.79$ Å, while (e)–(h) show Mn(X)-d, Mn(Y)-d, and Al-p PDOS of the tetragonal phase with lattice constants $a = 5.65$ Å and $c = 5.90$ Å. The value of $a = 5.65$ Å is chosen to be equal to that of the GaAs substrate.

polarization. Accordingly, our magnetic structure calculations confirm the half-metallicity and overall compensated magnetic moment in cubic phase Mn_3Al [4,7,13,14].

Recently, tetragonally-distorted thin films of related Heusler compounds have been grown epitaxially on GaAs (100), with an in-plane lattice constant $a = 5.65$ Å [25,26]. In our DFT calculations of Mn_3Al with tetragonal distortion, the c-lattice parameter is taken to be 5.90 Å. Despite the tetragonal distortion, our calculations reveal only a small change in magnetic moments with -2.61, 1.31, and $-0.02\mu_B$ on the Mn(X), Mn(Y), and Al atomic sites. respectively. In addition, the Mn(X)-d, Mn(Y)-d, and Al-p PDOS of the tetragonal phase shown in Figs. 2(e)–2(h) are very similar to the corresponding PDOS of the cubic phase. Therefore, the magnetic moments and PDOS results show half-metallic properties and almost fully compensated ferrimagnetic structures in both cubic and tetragonal phases of Mn_3Al. Therefore, these magnetic properties appear to be robust against small lattice distortions.

III. EXPERIMENTAL DETAILS

Mn_3Al thin films (50-nm nominal thickness) are grown on desorbed GaAs (001) substrates using an ultrahigh-vacuum MBE apparatus employing separate thermal-evaporation sources. The GaAs substrates undergo surface oxide removal via heating the substrate to 650 °C for 15 min in approximately 10^{-3}-Pa As flux [25]. Reflection high-energy electron-diffraction (RHEED) patterns indicate successful removal of the surface oxide. The Mn_3Al films are deposited epitaxially at 200 °C on the desorbed GaAs substrates. During the deposition, the RHEED pattern is collected to monitor the crystallographic ordering and alignment of the surface atoms. The thin films are further annealed after deposition at 300, 325, 350, and 400 °C for 30 min in ultrahigh vacuum (approximately 10^{-7} Pa) to investigate the effects of annealing on the structure. Scanning electron microscopy and energy-dispersive spectroscopy confirm the composition to be within 2% variation of the intended stoichiometry across the thin films. X-ray diffraction (XRD) measurements of the thin films are performed using a Cu-$K\alpha$ source with an average wavelength $\lambda = 1.5418$ Å. In addition, x-ray absorption spectroscopy is used to measure the valence states of the Mn d orbitals at beam line U4B at the National Synchrotron Light Source. Magnetic characterization is performed using a superconducting quantum-interference-device (SQUID) magnetometer with a maximum applied field of 5 T in the temperature range 5–400 K. For higher-temperature measurements (300–800 K), a vibrating sample magnetometer (VSM) is utilized. Resistivity measurements are carried out using a conductivity probe modified for use in the SQUID magnetometer [27]. The net in-plane magnetization of the thin films as a function of depth is deduced from the polarized-neutron-reflectometry (PNR) experiments carried out using the polarized beam reflectometer (PBR) beam line at the NIST Center for Neutron Research. The incident and scattered neutrons are spin polarized (>97% efficiency) to enable the determination of the parallel and perpendicular magnetization components with respect to applied field (700 mT at 100 K). The non-spin-flip components R^{++} and R^{--} (where $+/-$ refer to the neutron moment parallel or antiparallel to the applied field, respectively) can be used to determine the scattering length density depth profile which has nuclear (ρ_N) and magnetic (ρ_M proportional to the projection of the sample magnetization parallel to the applied field) contributions. REFL1D analysis software is used to refine the PNR model and fit the data [28,29].

IV. EXPERIMENTAL RESULTS

The growth-axis x-ray diffraction patterns of the Mn_3Al samples are shown in Fig. 3(a) as a function of the annealing temperature. The RHEED pattern shown in the inset of Fig. 3(a) indicates polycrystalline growth in

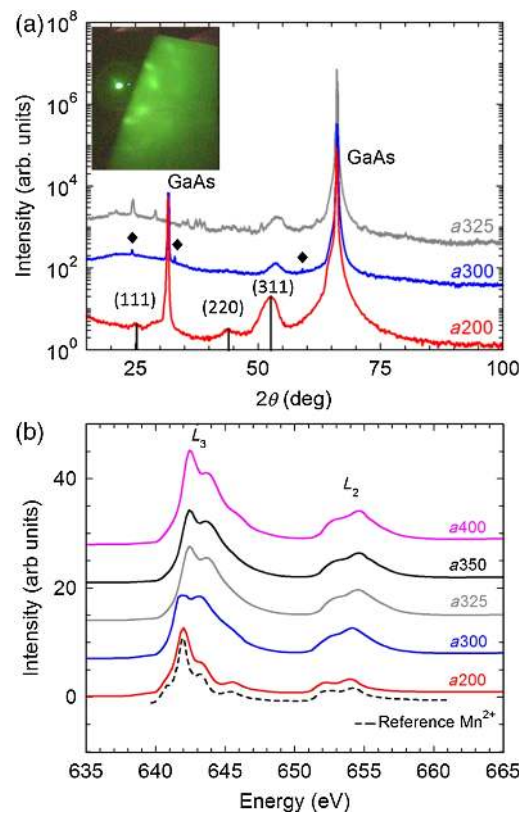

FIG. 3. (a) XRD of Mn_3Al as a function of the annealing temperature, indicating that the thin film is textured in the [311] direction. (Inset) The RHEED pattern indicates that the Mn_3Al grows on GaAs in a semipolycrystalline ordering as indicated by the ring of spots. (b) XAS curves for the Mn $L_{3,2}$ edges as a function of the annealing temperature. The a200 sample is in the Mn^{2+} valence state as confirmed by the reference spectrum from Qiao *et al.* [30]; however, there is a mixture of Mn^{2+} and Mn^{3+} states after the sample is annealed.

the as-grown sample [25]. The lattice constant for the as-grown state at 200 °C ($a200$) is found to be $a = 5.79 \pm 0.09$ Å, in excellent agreement with the predicted lattice constant in this work. As the annealing temperature is increased to 300 °C ($a300$), three sharp Bragg peaks emerge, as indicated by the diamond data markers, which may be attributed to mixing of the GaAs and Mn_3Al in the interfacial region. However, the (311) Bragg peak remains in the pattern, and the lattice constant is decreased to 5.68 ± 0.05 Å. The $D0_3$ lattice further deteriorates after the films are annealed to 325 °C (a325), indicated by the appearance of additional Bragg peaks in the XRD pattern. In the $a325$ pattern, more peaks emerge which can be indexed to α-Mn and Al, indicating that the lattice becomes more phase segregated.

X-ray absorption spectroscopy (XAS) aids in the structural analysis by providing information about changes in the Mn d-orbital occupancy at the L_3 and L_2 edges seen in Fig. 3(b) [31–34]. The comparison with the reference spectrum [30] reveals that the $a200$ sample has a pure valence state of Mn^{2+}. However, there is a change in valence states after annealing. It is seen that after annealing to 300 °C and higher, the relative Mn^{3+} contribution increases. The XAS, however, probes only the Mn surface layer and may not be indicative of the film as a whole [35]. Since there is an AlO_x capping layer to prevent thin-film oxidation, the change in the oxidation state suggested by the XAS data could be driven by oxygen infiltration into the Mn_3Al film during annealing, or it may reflect the additional interfacial oxygen at the Mn_3Al/AlO_x boundary. The Mn absorption edges are further discussed in the Supplemental Material [36].

The transport properties are measured as a function of temperature over 5–300 K. Figure 4(a) shows the zero-field resistivity $\rho_{xx}(T)$, which indicates semiconducting behavior. At low temperature, the resistivity is consistent with an intrinsic semiconductor in that the $\rho_{xx}(T)$ fits to the linear form $\rho_{xx} = \rho_0[1 + \gamma(T - T_0)]$, where γ is the temperature coefficient of resistivity, and T_0 is the reference temperature of 100 K. It is important to note that this model is valid only around the reference temperature, where γ is found to be -7.4×10^{-4} K^{-1}. However, at temperatures greater than 100 K, resistivity can be modeled as a sum of the metallic and semiconducting contributions [25]

$$\frac{1}{\rho_{xx}} = \sigma_{xx}(T) = n_m e\mu_m(T) + n_s e\mu_s(T), \qquad (1)$$

where m and s refer to the metallic and semiconducting components, respectively. The metallic carrier concentration n_m is taken to be a constant. The inverse mobilities are additive, as they represent series resistances and are given by $\mu_i^{-1} = (\alpha_i T + \beta_i)^{-1}$, where each conducting channel (metallic or semiconducting) i has different values for α and β. The α term results from electron-phonon scattering, while β corresponds to the mobility due to defects at

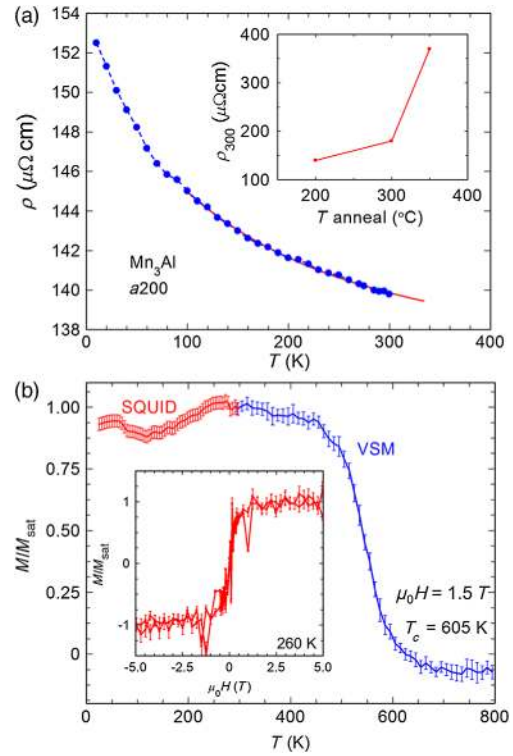

FIG. 4. (a) Electrical resistivity $\rho_{xx}(T)$ of the $a200$ sample. The red solid curve is fit to Eq. (1). Inset shows the ρ_{300} of the samples as a function of the annealing temperature, indicating that the resistivity increases as the samples are annealed at increasing temperatures, likely due to phase segregation. (b) Zero-field-cooled magnetometry data of the as-grown ($a200$) Mn_3Al thin film. The magnetization of the film saturates quickly as a function of increasing field (inset), and the Curie temperature is approximately 605 K.

$T = 0$ K. The fit assumes the number of thermally activated carriers varies as $n_s(T) = e^{-\Delta E/k_B T}$ with activation energy ΔE [25,37,38]. Fitting to this model [red solid curve in Fig. 4(a)] gives temperature coefficients α_m and α_s close to zero, suggesting that the mobility of Mn_3Al is heavily dominated by defect scattering rather than phonons. An activation energy of $\Delta E = 14 \pm 2$ meV is found. The room-temperature resistivity (ρ_{300}) as a function of the annealing temperature is measured for the $a200$, $a300$, and $a350$ samples and is shown in the inset in Fig. 4(a). The as-grown ($a200$) ρ_{300} value is 140 $\mu\Omega$ cm, which is close to values for Mn_2CoAl [25] and Cr_2CoGa [26]. The resistivity slightly increases after annealing for the $a300$ sample to 170 $\mu\Omega$ cm, but there is a dramatic increase to approximately 370 $\mu\Omega$ cm after annealing in the $a350$ sample. This rapid increase in ρ_{300} is consistent with the system becoming more disordered via phase segregation.

The magnetic moment is measured as a function of both field and temperature, with the magnetometry data displayed in Fig. 4(b). The increasing moment with increasing field for the as-grown ($a200$) sample (inset) is characteristic of a

ferrimagnet that is not totally compensated at 260 K. The temperature dependence of the saturation magnetization ($\mu_0 H = 1.5$ T) indicates that the as-grown sample has a Curie temperature (T_C) of 605 K. The small change in magnetization of the film below 200 K can possibly arise from subtle changes in the film's magnetocrystalline anisotropy at low temperatures.

The magnetic moment measured using the SQUID as well as VSM magnetometers has a large diamagnetic contribution from the substrate, inhibiting the accurate determination of the absolute moment per formula unit (f.u.). To remedy this issue, PNR is used to probe the net magnetization in the Mn_3Al layer for the $a200$ and $a300$ samples. Figure 5(a) displays the R^{++} and R^{--} reflectivities as a function of the wave-vector transfer Q for the $a200$ sample at 100 K under an applied field of 0.7 T. The spin asymmetry (SA) emphasizes the magnetic contribution to scattering and is calculated by

$$\mathrm{SA} = \frac{R^{++} - R^{--}}{R^{++} + R^{--}}, \tag{2}$$

and shown in Fig. 5(b).

Figure 5(c) shows the structural (ρ_N) and magnetic (ρ_M) scattering length profiles obtained from the best fits of the reflectometry data [solid lines in Fig. 5(a)]. In the nuclear profile, there is evidence of a distinct interface layer between the GaAs and Mn_3Al layers (assumed unmagnetized in our model) caused by incomplete desorption of the substrate. The results obtained from the best fit to the data are consistent with the existence of a magnetic dead layer of thickness 8.9 ± 2.8 nm adjacent to the interface layer [Fig. 5(c)]. The magnetization calculated from the fit is 23 ± 8 emu/cm^3 (1 emu = 1 kA m^{-1}), consistent with a small magnetic moment in the relevant layer corresponding to 0.11 ± 0.04 μ_B/f.u. While the fit shown in Figs. 5(a) and 5(b) best captures the features of the measured reflectivity and spin asymmetry, there is a distribution in the fitted values for the thickness of the magnetic dead layer. The error in value is, thus, estimated by exploring a series of models that describes the data reasonably well, as discussed in the Supplemental Material [36]. The measured magnetization is greater than the corresponding theoretical value possibly due to the presence of paramagnetic Mn crystallites or a secondary magnetic phase in our samples. Alternative fits that support the choice of the best fit for the $a200$ sample and the fit used for the $a300$ sample are provided in the Supplemental Material [36]. The PNR results indicate that the Mn_3Al magnetic moment for $a300$ corresponds to a value 30 ± 5 emu/cm^3 (0.15 ± 0.03 μ_B/f.u.).

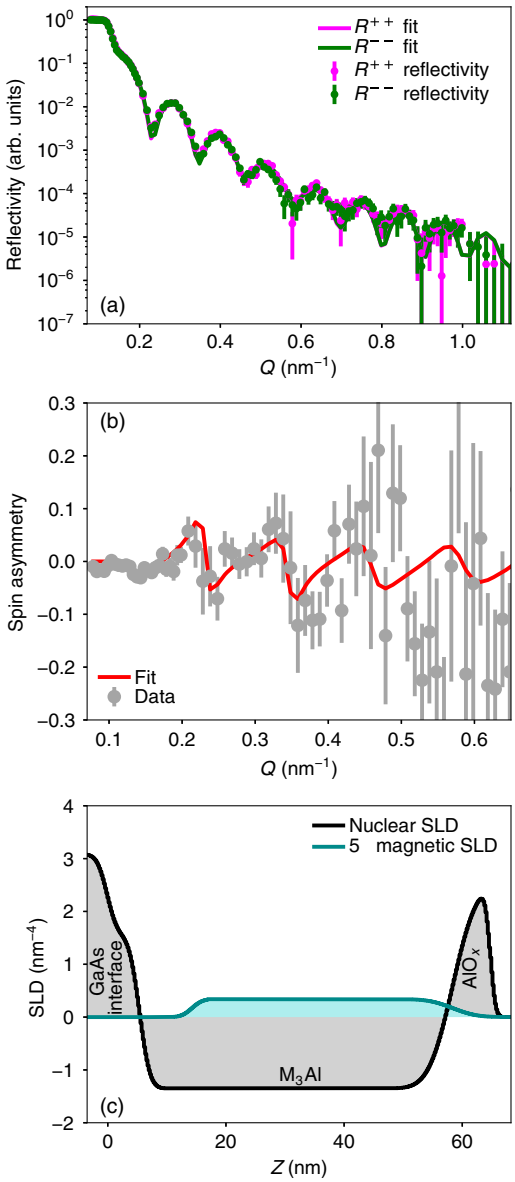

FIG. 5. (a) R^{++} and R^{--} reflectivities from the $a200$ sample as a function of $Q_{\bar{z}}$. (b) Spin asymmetry of the reflectometry data, which tracks the magnetization within the Mn_3Al layer parallel to the applied field. (b) Profiles of the nuclear (ρ_N) and magnetic (ρ_M) scattering length density (SLD) as a function of depth (z).

V. CONCLUSION

Compensated ferrimagnetism in $D0_3$ Mn_3Al is computationally and experimentally confirmed in study. The first-principles analysis yields a low net magnetization of $0.017\mu_B$/f.u. at a lattice constant of $a = 5.79$ Å. X-ray diffraction measurements show the presence of strong [311] texturing of the $D0_3$ structure. Mn L-edge x-ray absorption spectroscopy reveals that the valence state is Mn^{2+} in the as-grown sample, and the valence state increases as the annealing temperature increases. Electrical transport of the material behaves as a semiconductor at low temperatures, but above 100 K, it displays a combined semiconductor-metallic form, which involves low-energy states with an activation energy of 14 meV. The resistivity at room temperature increases after the sample is annealed, consistent with the notion that the Mn_3Al lattice becomes phase segregated after annealing at 300 °C. The magnetization

measurements determine a high T_C value of 605 K, while the PNR measurements reveal a weak net magnetization of $0.11 \pm 0.04\ \mu_B$ in the Mn_3Al layer. The successful growth and stabilization of a Heusler compound with nearly zero net magnetization opens material opportunities for spintronics applications.

ACKNOWLEDGMENTS

We thank T. Hussey for assistance with magnetometry, D. Gilbert, B. A. Assaf, and C. A. Lane for helpful discussions, and G. Player and M. C. DeCapua for general assistance. The experimental work at Northeastern University is supported by the National Science Foundation Grant No. ECCS-1402738. The work of the AB group at Northeastern University is supported by the U.S. Department of Energy (DOE), Office of Science, Basic Energy Sciences Grant No. DE-FG02-07ER46352 (core research), and benefits from Northeastern University's Advanced Scientific Computation Center, the NERSC supercomputing center through DOE Grant No. DE-AC02-05CH11231, and support (applications to layered materials) from the DOE EFRC: Center for the Computational Design of Functional Layered Materials under Grant No. DE-SC0012575.

[1] J. M. D. Coey, *Magnetism and Magnetic Materials*, 1st ed. (Cambridge University Press, Cambridge, England, 2009).

[2] H. Kurt, K. Rode, P. Stamenov, M. Venkatesan, Y.-C. Lau, E. Fonda, and J. M. D. Coey, Cubic Mn_2Ga hin Films: Crossing the Spin Gap with Ruthenium, Phys. Rev. Lett. **112**, 027201 (2014).

[3] M. E. Jamer, L. G. Marshall, G. E. Sterbinsky, L. H. Lewis, and D. Heiman, Low-moment ferrimagnetic phase of the Heusler compound Cr_2CoAl, J. Magn. Magn. Mater. **394**, 32 (2015).

[4] S. Wurmehl, H. C. Kandpal, G. Fecher, and C. Felser, Valence electron rules for prediction of half-metallic compensated-ferrimagnetic behaviour of Heusler compounds with complete spin polarization, J. Phys. Condens. Matter **18**, 6171 (2006).

[5] X. L. Wang, Proposal for a New Class of Materials: Spin Gapless Semiconductors, Phys. Rev. Lett. **100**, 156404 (2008).

[6] H. Hakimi, M. Venkatesan, K. Rode, K. Ackland, and J. M. D. Coey, The zero-magnetization Heusler ferrimagnet, J. Appl. Phys. **113**, 17B101 (2013).

[7] G. Y. Gao and K. L. Yao, Antiferromagnetic half-metals, gapless half-metals, and spin gapless semiconductors: The $D0_3$-type Heusler alloys, Appl. Phys. Lett. **103**, 232409 (2013).

[8] M. E. Jamer, B. A. Assaf, G. E. Sterbinsky, D. Arena, L. H. Lewis, and A. A. Saúl, G. Radtke, and D. Heiman, Antiferromagnetic phase of the gapless semiconductor V_3Al, Phys. Rev. B **91**, 094409 (2015).

[9] I. Galanakis, S. Tirpanci, and K. Özdoğan, and E. Sasiğlu, Itinerant G-type antiferromagnetism $D0_3$-type V_3Z (Z = Al, Ga, In) compounds: A first-principles study, Phys. Rev. B **94**, 064401 (2016).

[10] A. Bansil, S. Kaprzyk, P. E. Mijnarends, and J. Toboła, Electronic structure and magnetism of $Fe_{3-x}V_xX$ (X = Si, Ga, and Al) alloys by the KKR-CPA method, Phys. Rev. B **60**, 13396 (1999).

[11] X. T. Wang, Z. X. Cheng, J. L. Wang, X. L. Wang, and G. D. Liu, A full spectrum of spintronic properties demonstrated by a $C1_b$-type Heusler compound Mn_2Sn subjected to strain engineering, J. Mater. Chem. C **4**, 8535 (2016).

[12] X. L. Wang, S. X. Dou, and C. Zhang, Zero-gap materials for future spintronics, electronics and optics, NPG Asia Mater. **2**, 31 (2010).

[13] H. Luo, Z. Zhu, L. Ma, S. Xu, Z. Zhu, C. Jiang, H. Xu, and G. Wu, Effect of site preference of 3*d* atoms on the electronic structure and half-metallicity of Heusler alloy Mn_2YAl, J. Phys. D **41**, 055010 (2008).

[14] S. M. Azar, B. A. Hamad, and J. M. Khalifeh, Structural, electronic and magnetic properties of $Fe_{3-x}Mn_xZ$ (Z = Al, Ge, Sb) Heusler alloys, J. Magn. Magn. Mater. **324**, 1776 (2012).

[15] S. Skaftouros, K. Özdoğan, E. Sasiğlu, and I. Galanakis, Search for spin gapless semiconductors: The case of inverse Heusler compounds, Appl. Phys. Lett. **102**, 022402 (2013).

[16] S. Skaftouros, K. Özdoğan, E. Sasiğlu, and I. Galanakis, Generalized Slater-Pauling rule for the inverse Heusler compounds, Phys. Rev. B **87**, 024420 (2013).

[17] A. K. Nayak, M. Nicklas, S. Chadov, P. Khuntia, C. Shekhar, A. Kalache, M. Baenitz, Y. Skourski, V. K. Guduru, A. Puri, U. Zeitler, J. M. D. Coey, and C. Felser, Design of compensated ferrimagnetic Heusler alloys for giant tunable exchange bias, Nat. Mater. **14**, 679 (2015).

[18] D. Betto, K. Rode, N. Thiyagarajah, Y. C. Lau, K. Borisov, G. Atcheson, M. Zic, T. Archer, P. Stamenov, and J. M. D. Coey, The zero-moment half metal: How could it change spin electronics, AIP Adv. **6**, 055601 (2016).

[19] G. Kresse and D. Joubert, From ultrasoft pseudopotentials to the projector augmented-wave method, Phys. Rev. B **59**, 1758 (1999).

[20] J. P. Perdew, K. Burke, and M. Ernzerhof, Generalized Gradient Approximation Made Simple, Phys. Rev. Lett. **77**, 3865 (1996).

[21] G. Kresse and J. Hafner, *Ab initio* molecular dynamics for open-shell transition metals, Phys. Rev. B **48**, 13115 (1993).

[22] B. Barbiellini, E. G. Moroni, and T. Jarlborg, Effects of gradient corrections on electronic structure in metals, J. Phys. Condens. Matter **2**, 7597 (1990).

[23] C. L. Fu and K. M. Ho, First-principles calculation of the equilibrium ground-state properties of transition metals: Applications to Nb and Mo, Phys. Rev. B **28**, 5480 (1983).

[24] F. D. Murnaghan, The compressibility of media under extreme pressures, Proc. Natl. Acad. Sci. U.S.A. **30**, 244 (1944).

[25] M. E. Jamer, B. A. Assaf, T. Devakul, and D. Heiman, Magnetic and transport properties of Mn_2CoAl oriented films, Appl. Phys. Lett. **103**, 142403 (2013).

[26] M. E. Jamer, G. E. Sterbinsky, G. M. Stephen, M. C. DeCapua, G. Player, and D. Heiman, Magnetic properties of low-moment ferrimagnetic Heusler Cr_2CoGa thin films grown by molecular beam epitaxy, Appl. Phys. Lett. **109**, 182402 (2016).

[27] B. A. Assaf, T. Cardinal, P. Wei, F. Katmis, J. S. Moodera, and D. Heiman, Modified electrical transport probe design for standard magnetometer, Rev. Sci. Instrum. **83**, 033904 (2012).

[28] B. J. Kirby, P. A. Kienzle, B. B. Maranville, N. F. Berk, K. J. Krycka, F. Heinrich, and C. F. Majkrzak, Phase-sensitive specular neutron reflectometry for imaging the nanometer scale composition depth profile of thin-film materials, Curr. Opin. Colloid Interface Sci. **17**, 44 (2012).

[29] NCNR, MS Windows NT kernel description, 2016, https://www.ncnr.nist.gov/instruments/ng1refl/.

[30] R. Qiao, T. Chin, S. J. Harris, S. Yan, and W. Yang, Spectroscopic fingerprints of valence and spin states in manganese oxides and fluorides, Curr. Appl. Phys. **13**, 544 (2013).

[31] B. T. Thole, P. Carra, F. Sette, and G. van der Laan, X-Ray Circular Dichroism as a Probe of Orbital Magnetization, Phys. Rev. Lett. **68**, 1943 (1992).

[32] G. van der Laan and I. W. Kirkman, The 2p absorption spectra of 3*d* transition metal compounds in tetrahedral and octahedral symmetry, J. Phys. Condens. Matter **4**, 4189 (1992).

[33] P. Carra, B. T. Thole, M. Altarelli, and X. Wang, X-Ray Circular Dichroism and Local Magnetic Fields, Phys. Rev. Lett. **70**, 694 (1993).

[34] H. K. Schmid and W. Mader, Oxidation states of Mn and Fe in various compound oxide systems, Micron **37**, 426 (2006).

[35] B. Ravel and M. Newville, ATHENA, ARTEMIS, HEPHAESTUS: Data analysis for x-ray absorption spectroscopy using IFEFFIT, J. Synchrotron Radiat. **12**, 537 (2005).

[36] See Supplemental Material at http://link.aps.org/supplemental/10.1103/PhysRevApplied.7.064036 for PNR and XAS details.

[37] L. Bainsla, A. I. Mallick, M. M. Raja, A. A. Coelho, A. K. Nigam, D. D. Johnson, A. Alam, and K. G. Suresh, Origin of spin gapless semiconductor behavior in CoFeCrGa: Theory and experiment, Phys. Rev. B **92**, 045201 (2015).

[38] L. Bainsla, A. I. Mallick, A. A. Coelho, A. K. Nigam, B. S. D. Varaprasad, Y. K. Takahashi, A. Alam, K. G. Suresh, and K. Hono, High spin polarization and spin splitting in equiatomic quaternary CoFeCrAl Heusler alloy, J. Magn. Magn. Mater. **394**, 82 (2015).